Differential impact of a-Nb_2O_5 and a-TiO_2 ETL on the photoelectric performance of $Cs_3Sb_2I_{9-x}Cl_x$ perovskite solar cells

FEI ZHAO[1,*], PEIZHI YANG[2,*], JUNHAO CHU[3]
[1]*School of Photoelectric Engineering, Changzhou Institute of Technology, Changzhou, Jiangsu, 213002, China*
[2]*Key Laboratory of Advanced Technique & Preparation for Renewable Energy Materials, Ministry of Education, Yunnan Normal University, Kunming 650500, China*
[3]*Shanghai Institute of Technical Physics, Chinese Academy of Sciences, Shanghai 200083, China*

Recently, the stable all-inorganic lead-free $Cs_3Sb_2I_{9-x}Cl_x$ perovskite-like solar cells have attracted enormous attention where the electron transport layer (ETL) is extremely important. Herein, the amorphous Nb_2O_5 (a-Nb_2O_5) ETL was prepared by sputtering technology at room temperature to increase the optical band gap of a-Nb_2O_5 layer, improve its conduction band minimum (CBM), suppress charge recombination at the a-Nb_2O_5/$Cs_3Sb_2I_{9-x}Cl_x$ interface, and reduce leakage current of $Cs_3Sb_2I_{9-x}Cl_x$ solar cells. More importantly, the a-Nb_2O_5-based $Cs_3Sb_2I_{9-x}Cl_x$ solar cell presents a higher efficiency (1.75 %) compared with $Cs_3Sb_2I_{9-x}Cl_x$ device containing a-TiO_2 ETL (0.69 %). Additionally, the a-Nb_2O_5 ETL increases the device stability in air. This study highlights the great effect of a-Nb_2O_5 ETL as a carrier controller on enhancing performance of $Cs_3Sb_2I_{9-x}Cl_x$ solar cells.

(Received December 31, 2022; accepted August 10, 2023)

Keywords: Amorphous Nb_2O_5, Electron transport layer, Charge recombination, Lead-free $Cs_3Sb_2I_{9-x}Cl_x$ solar cells

1. Introduction

Metal halide perovskite semiconductors comprising interesting photoelectric properties have indicated great potential for high-performance photovoltaics [1-5]. In just over a decade, inorganic-organic hybrid perovskite solar cells (PSCs) have achieved an unprecedented rate of development with a current certified power conversion efficiency (PCE) exceeding 25.5% [6]. However, the instability of organic-inorganic halide PSCs against moisture and temperature remains a major obstacle to its application [7, 8]. The study of all inorganic $CsPbBr_3$ PSCs is conducive to improving the stability of traditional halide perovskite devices [9, 10]. Despite the excellent stability of $CsPbBr_3$ PSCs, the absorber in $CsPbBr_3$ devices contains toxic Pb element, which seriously affects the surrounding environment. Therefore, it is crucial to seek a nontoxic and stable perovskite solar cell.

Recently, all-inorganic $Cs_3Sb_2I_9$ perovskite-like solar cell has also attracted significant interest, which is due to the high absorption coefficient, non-toxicity and excellent moisture and heat stability of the absorber [1]. Singh et al. deposited all-inorganic $Cs_3Sb_2I_9$ film by a vapor-assisted solution technique and manufacture $Cs_3Sb_2I_9$-based solar cells containing an efficiency of 1.5% [11]. In the aforementioned article, the study indicated that the quality of the absorber is important to the device performance improvement. In addition to the absorbing layer, the electron transport layer (ETL) in all-inorganic $Cs_3Sb_2I_9$ solar cell can play the role of transporting electrons and suppressing holes, which greatly affects the cell performance. Umar et al. [12] used TiO_2 as ETL for $Cs_3Sb_2I_9$ cell and they achieved a device efficiency of 1.2 %. In this study, the ETL adopted in $Cs_3Sb_2I_9$ device is TiO_2. TiO_2 presents low electron mobility (~1 $cm^2V^{-1}s^{-1}$), which impedes the device performance improvement. Herein, it is imperative to find the ETL including outstanding optoelectronic properties. The Nb_2O_5 containing large optical band gap (>3 eV) and high electron mobility has been used in organic-inorganic halide solar cell and all-inorganic solar cell. Shen et al. [13] prepared crystalline Nb_2O_5 (c-Nb_2O_5) film through a solution deposited technique and fabricate c-Nb_2O_5-based organic-inorganic halide PSC with a 19.2 % efficiency. Furthermore, Guo et al. [14] synthesized c-Nb_2O_5 film as ETL via sputtering method at high temperature for all-inorganic lead-free $Cs_3Sb_2I_{9-x}Cl_x$ solar cells and realized efficiency over 1.9 %. However, to the best of our knowledge, no study has been reported on adopting amorphous Nb_2O_5 (a-Nb_2O_5) film as ETL for all-inorganic $Cs_3Sb_2I_{9-x}Cl_x$ device.

In this work, we deposited a-Nb_2O_5 film by a simple

sputtering technology at room temperature and fabricated a-Nb_2O_5-based lead-free $Cs_3Sb_2I_{9-x}Cl_x$ solar cells. For comparison, amorphous TiO_2 (a-TiO_2) film also was prepared via same sputtering technique at same temperature. Best-performance efficiency of the $Cs_3Sb_2I_{9-x}Cl_x$ cell including a-Nb_2O_5 film has attained to 1.75 %, which is higher than the efficiency of the $Cs_3Sb_2I_{9-x}Cl_x$ cell containing a-TiO_2 film (0.69 %). The enhanced photovoltaic properties of a-Nb_2O_5-based devices are due to the large optical band gap and high conduction band minimum (CBM) of a-Nb_2O_5 and fast carrier extraction capability at the a-Nb_2O_5/$Cs_3Sb_2I_{9-x}Cl_x$ interface. In addition, the $Cs_3Sb_2I_{9-x}Cl_x$ cell with a-Nb_2O_5 shows an excellent moisture tolerance in air. Adopting a-Nb_2O_5 film as ETL may give a novel path to produce high-efficiency and stable $Cs_3Sb_2I_{9-x}Cl_x$ solar cells.

2. Experimental

2.1. Deposition of thin films

The amorphous Nb_2O_5 films were prepared on FTO substrates by sputtering technology. When the vacuum pressure is pumped to 5×10^{-4} Pa, only Ar is introduced into the chamber, and the Ar flow rate is 20 sccm. The working pressure is 0.3 Pa and the substrate temperature was set to room temperature. The deposition power and deposition time was set to 150 W and 25 min, respectively. After setting all parameters, an amorphous Nb_2O_5 films was prepared successfully. For depositing amorphous TiO_2 films, the TiO_2 films were deposited on substrates by same sputtering technology at room temperature. The vacuum pressure, Ar flow rate, working pressure, deposition power and deposition time were 5×10^{-4} Pa, 20 sccm, 0.3 Pa, 150 W and 20 min, respectively. Next, 0.75 M CsI, 0.25 M SbI_3 and 0.3125 M $SbCl_3$ were mixed in DMF, which can form the $Cs_3Sb_2Cl_xI_{9-x}$ precursor solution. Then, $Cs_3Sb_2Cl_xI_{9-x}$ precursor solution was deposited on amorphous Nb_2O_5 and TiO_2 films. The deposition speed and time are 3000rpm and 30s, respectively. The anisole (65 μL) was immediately dropped on the $Cs_3Sb_2Cl_xI_{9-x}$ precursor after depositing 8 s. Then, the $Cs_3Sb_2Cl_xI_{9-x}$ samples were annealed at 230 ℃ for 10 min through using a SbI_3 vapor heating technology. The P3HT films were then deposited on the $Cs_3Sb_2Cl_xI_{9-x}$ film at 3000 rpm for 60 s and heated at 120 ℃ for 5 min. Finally, the carbon paste was prepared by a screen printing technology.

2.2. Characterizations

The crystal structure and phases were tested through XRD using Cu K α radiation. X-ray photoelectron spectroscopy (XPS) spectra were acquired by using an Al Kα X-ray source. The absorption spectra were characterized adopting UV-vis spectrophotometer. The morphology and microstructure were gained through SEM. The PL was applied to test film emissions in which light source was a xenon lamp. The current density-voltage (J-V) characteristics were tested under simulated AM1.5G (100 mW/cm^2) illumination. The incident photo-to-current conversion efficiency (IPCE) measurements were taken through a homemade setup and Newport monochromator. The active area of cell is 0.09 cm^2.

3. Results and discussions

3.1. Film structure

In order to study the growth of TiO_2 and Nb_2O_5 films deposited at room temperature, we performed XRD characterization of the TiO_2 and Nb_2O_5 films. From the XRD pattern of Fig. 1a, there are no diffraction peaks for TiO_2 and Nb_2O_5 films, indicating that both films have amorphous properties [15].

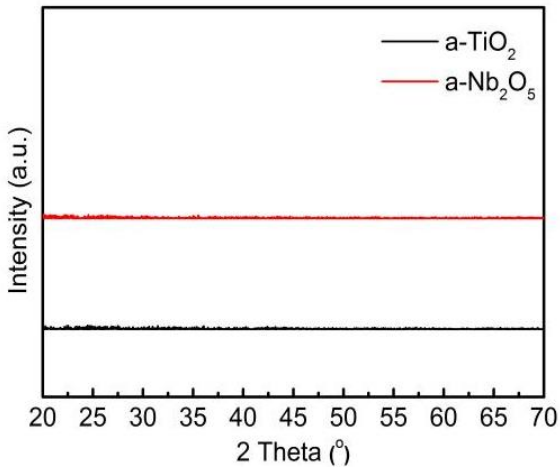

Fig. 1. XRD patterns of a-TiO_2 and a-Nb_2O_5 films deposited on glass substrates (color online)

Fig. 2a and Fig. 2b show the Ti 2p spectrum of a-TiO_2 film and the Nb 3d spectrum of a-Nb_2O_5 film, respectively. The peaks of pure a-TiO_2 film located at 458.0 eV and 463.7 eV demonstrate the spin-orbit splitting of the Ti 2p components ($2p_{3/2}$ and $2p_{1/2}$, separately) [16]. The peaks of pure a-Nb_2O_5 layer located at 206.6 eV and 209.3 eV show the spin-orbit splitting of the Nb 3d components ($3d_{5/2}$ and$3d_{3/2}$, separately) [15]. In addition, the O 1s peaks of a-TiO_2 film and a-Nb_2O_5 film (Fig. 2c and Fig. 2d) are located at 529.4 eV and 529.5 eV [16, 17], which indicates a chemical shift of 0.1 eV. The aforementioned research results show that we have successfully prepared a-TiO_2 and a-Nb_2O_5 films.

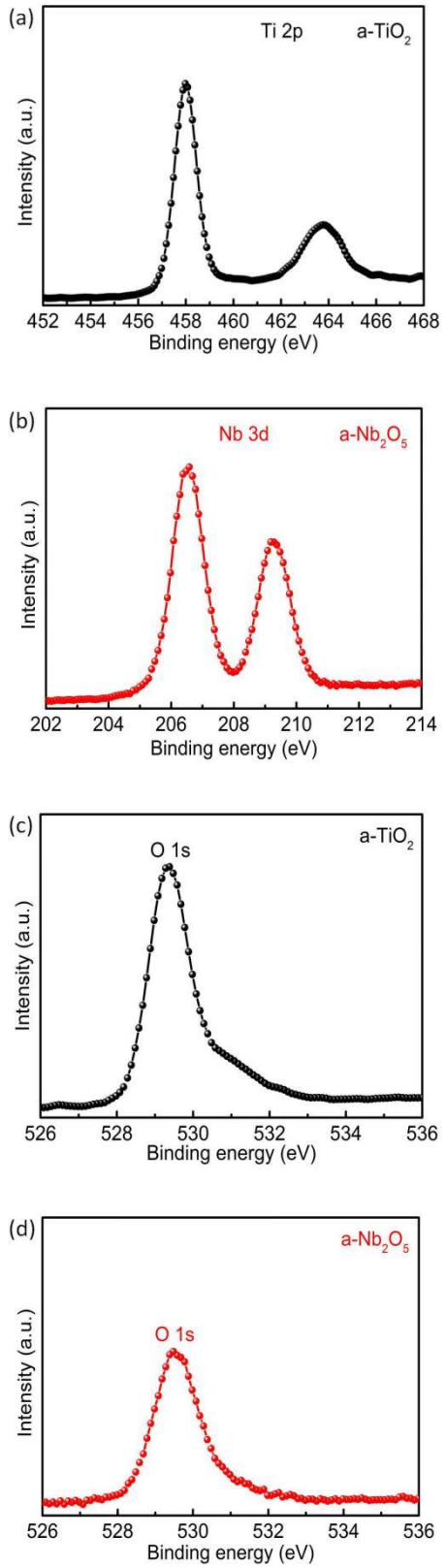

Fig. 2. (a) XPS spectrum (Ti 2p) of a-TiO_2. (b) XPS spectrum (Nb 3d) of a-Nb_2O_5. XPS spectra (O 1s) of (c) a-TiO_2 and (d) a-Nb_2O_5 (color online)

3.2. Optical properties

Fig. 3a indicates the absorption spectra of a-TiO_2 and a-Nb_2O_5 films. Compared with a-TiO_2, The absorption edge of the a-Nb_2O_5 film is blue-shifted, implying that its optical band gap becomes larger. The band gaps of a-TiO_2 and a-Nb_2O_5 films are seen in Fig. 3b. For a-TiO_2 film, it presents a band gap value of 3.52 eV. However, a-Nb_2O_5 film presents a larger band gap value (3.66 eV). This is consistent with the previous analysis results. A larger value of the band gap for a-Nb_2O_5 film is beneficial to the sufficient absorption of sunlight by the absorber, which can further improve cell performance.

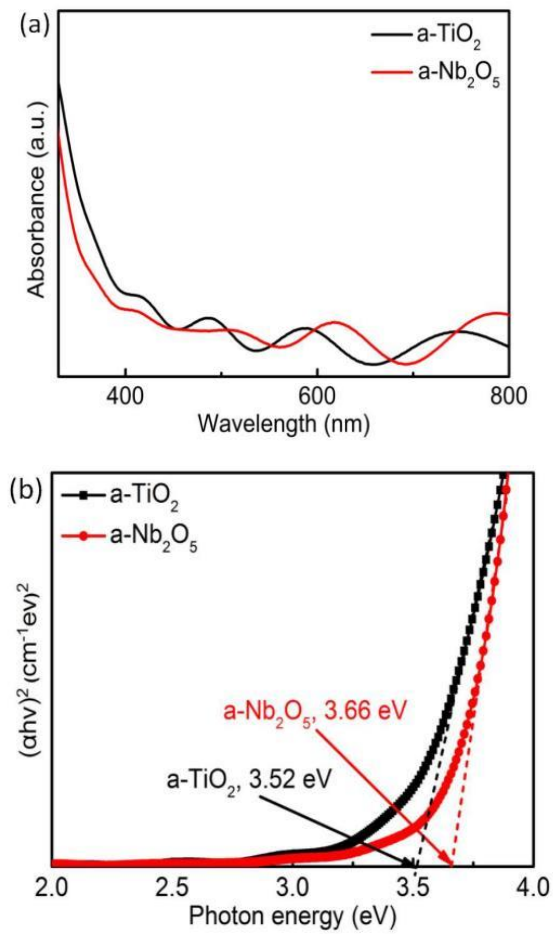

Fig. 3. (a) Absorption spectra of a-TiO_2 and a-Nb_2O_5. (b) Band gaps of various samples (color online)

3.3. Cross-sectional characterization

Fig. 4a indicates the schematic structure of $Cs_3Sb_2I_{9-x}Cl_x$ solar cell. The $Cs_3Sb_2I_{9-x}Cl_x$ solar cell consists of FTO, a-Nb_2O_5 ETL, $Cs_3Sb_2I_{9-x}Cl_x$ absorber, P3HT layer and carbon. Fig. 4b shows the cross-sectional SEM image of $Cs_3Sb_2I_{9-x}Cl_x$ device. It can be observed from the Fig. 4b that there is a good contact between layers, showing that the whole cell possesses great quality [18].

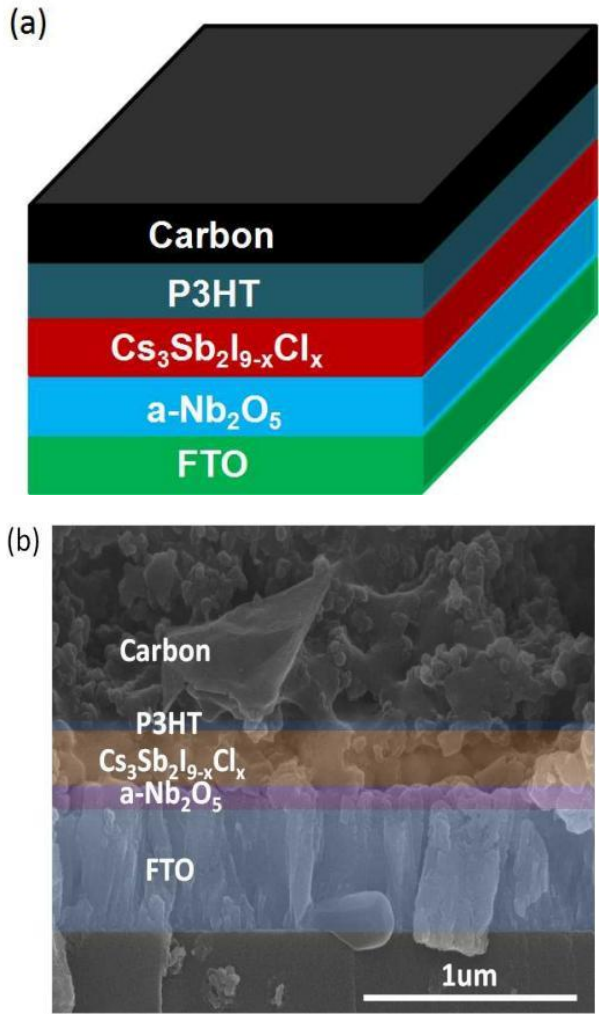

Fig. 4. (a) Schematic structure of $Cs_3Sb_2I_{9-x}Cl_x$ solar cell. (b) Cross-sectional SEM image of $Cs_3Sb_2I_{9-x}Cl_x$ solar cell (color online)

3.4. Device characterization

To investigate the influence of ETLs including various sputtering time on the properties of inorganic $Cs_3Sb_2I_{9-x}Cl_x$ solar cells, the J-V curves and related test results of $Cs_3Sb_2I_{9-x}Cl_x$ cells containing a-TiO_2 layers based on various sputtering time are described in Fig. 5a and Table 1, separately. The $Cs_3Sb_2I_{9-x}Cl_x$ cell efficiency enhances from 0.57 % to 0.69 % as the sputtering time of a-TiO_2 enhances from 15 min to 20 min. When the a-TiO_2 sputtering time further increases to 25 min, the device efficiency decreases to 0.55 %. These results show that optimal sputtering time for a-TiO_2 is 20 min. Fig. 5b shows the J-V characteristics of solar cells containing a-Nb_2O_5 ETLs with various sputtering time. Table 2 indicates corresponding photovoltaic parameters in Fig. 5b. When the sputtering time of a-Nb_2O_5 is 20 min, the $Cs_3Sb_2I_{9-x}Cl_x$ cell efficiency is 1.48%. As the a-Nb_2O_5 sputtering time further increases to 25 min, the cell efficiency increases to 1.75%. However, when the a-Nb_2O_5 sputtering time increases to 30 min, the device efficiency decreases to 1.66 %. These results indicate that optimal sputtering time for a-Nb_2O_5 is 25 min.

Fig. 5c gives the J-V curves of the optimized solar cells with a-TiO_2 and a-Nb_2O_5. Table 3 indicates corresponding photovoltaic parameters in Fig. 5c. The efficiencies of a-TiO_2-based and a-Nb_2O_5-based cells are 0.69 % and 1.75%, respectively. This suggests that a-Nb_2O_5-based cell possesses higher efficiency in comparison to a-TiO_2-based device.The main reason for the improved efficiency of a-Nb_2O_5-based cells is due to the improvement of open circuit voltage (V_{oc}), short circuit current density (J_{sc}) and fill factor (FF). The IPCE spectra for two devices with both a-TiO_2 and a-Nb_2O_5 are presented in Fig. 5d. A significantly higher IPCE can be observed for device with a-Nb_2O_5 film compared with that of device containing a-TiO_2 film. The calculated J_{sc} from the IPCE are 2.52 mA/cm^2 and 3.72 mA/cm^2 for device with a-TiO_2 and a-Nb_2O_5, respectively. This indicates the calculated J_{sc} of a-Nb_2O_5-based device is higher than that of a-TiO_2-based device, which is consistent with the previous analysis results.

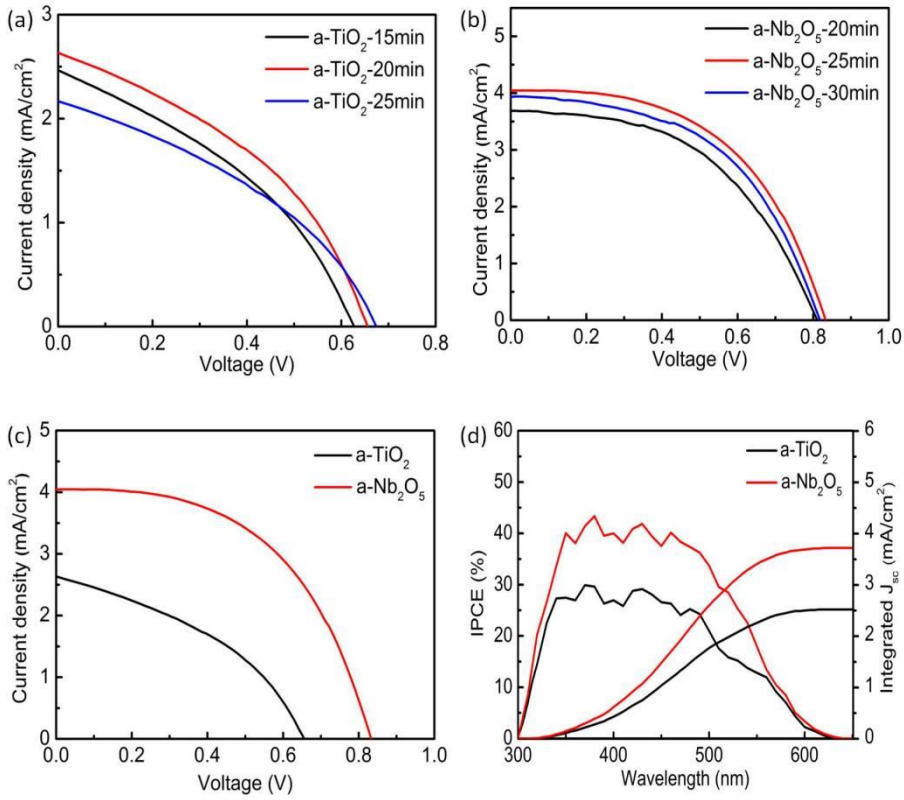

Fig. 5. (a) J-V characteristics of $Cs_3Sb_2I_{9-x}Cl_x$ cells containing a-TiO_2 ETLs with various sputtering time; (b) J-V characteristics of $Cs_3Sb_2I_{9-x}Cl_x$ cells containing a-Nb_2O_5 ETLs with various sputtering time; (c) J-V curves of cells based on a-TiO_2 and a-Nb_2O_5. (d) IPCE spectra of $Cs_3Sb_2I_{9-x}Cl_x$ cells including various ETLs (color online)

Table 1. The related parameters of the $Cs_3Sb_2I_{9-x}Cl_x$ cells containing a-TiO_2 with various sputtering time

Sputtering time	V_{oc} (V)	J_{sc} (mA/cm^2)	FF	PCE (%)
15 min	0.62	2.46	0.37	0.57
20 min	0.65	2.63	0.40	0.69
25 min	0.67	2.17	0.38	0.55

Table 2. The related parameters of the $Cs_3Sb_2I_{9-x}Cl_x$ cells based on a-Nb_2O_5 with different sputtering time

Sputtering time	V_{oc} (V)	J_{sc} (mA/cm^2)	FF	PCE (%)
20 min	0.81	3.69	0.50	1.48
25 min	0.83	4.04	0.52	1.75
30 min	0.82	3.94	0.52	1.66

Table 3. The related parameters of the $Cs_3Sb_2I_{9-x}Cl_x$ cells based on a-TiO_2 and a-Nb_2O_5 layers

ETL	V_{oc} (V)	J_{sc} (mA/cm^2)	FF	PCE (%)
a-TiO_2	0.65	2.63	0.40	0.69
a-Nb_2O_5	0.83	4.04	0.52	1.75

Fig. 6 is box charts exhibiting the statistical features (PCE) of the carbon-based $Cs_3Sb_2I_{9-x}Cl_x$ solar cells with a-TiO_2 and a-Nb_2O_5. It is obvious that the PCE is enhanced after using a-Nb_2O_5, which reveals an outstanding reproducibility for inorganic lead-free antimony-based perovskite-inspired solar cells [19].

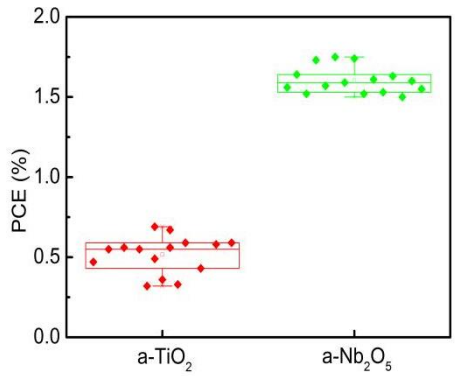

Fig. 6. Statistical distribution of the PCEs for the $Cs_3Sb_2I_{9-x}Cl_x$ cells containing different ETLs (color online)

The related J-V test results for $Cs_3Sb_2I_{9-x}Cl_x$ cells with a-Nb_2O_5 ETL under different sweep directions are shown in Fig. 7a. The a-Nb_2O_5-based $Cs_3Sb_2I_{9-x}Cl_x$ cell displays a V_{oc} of 0.83 V, a FF of 0.52, and a PCE of 1.75 % under the reverse sweep direction. However, when the device was tested under forward scan conditions, its V_{oc}, FF, and PCE dropped to 0.76 V, 0.45, and 1.32 %, respectively. The difference between reverse scan and forward scan implies the presence of hysteretic behavior.

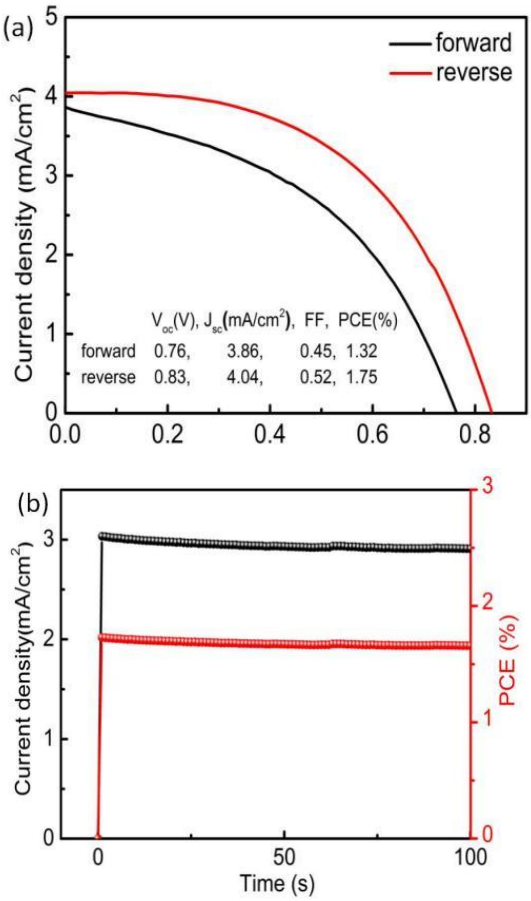

Fig. 7. (a) a-Nb_2O_5 ETL under different sweep directions. (b) Steady output PCE of devices based on a-Nb_2O_5 ETL (color online)

The hysteresis behavior for the $Cs_3Sb_2I_{9-x}Cl_x$ cell containing a-Nb_2O_5 originates from the difference between the rate of electron transfer from the absorber to the a-Nb_2O_5 layer and the rate of hole transfer from the absorber to the P3HT layer [13]. The photocurrent and efficiency outputs at the maximum power point are recorded to estimate the efficiency of the cell accurately [20]. As seen in Fig. 7b, the current and efficiency outputs of the best-performing cells rise up quickly to the maximum once the light is turned on. A stabilized efficiency of 1.66% containing a current density of 2.91 mA/cm^2 is gained at an applied voltage bias of 0.57 V for the a-Nb_2O_5-based cells. This indicates that this efficiency value is very similar to the one obtained from the J-V curve.

Fig. 8a shows plot of dJ/dV vs V. The shunt conductance (G) value for lead-free solar cells with a-TiO_2 and a-Nb_2O_5 are 2.01 mS/cm^2 and 0.10 mS/cm^2, respectively. The reduced G value for a-Nb_2O_5-based lead-free solar cells indicates that the device possesses better performance [21, 22]. Fig. 8b gives the energy band diagrams of $Cs_3Sb_2I_{9-x}Cl_x$ cells containing a-TiO_2 and a-Nb_2O_5. The conduction band minimum (CBM) values for a-TiO_2, a-Nb_2O_5 and $Cs_3Sb_2I_{9-x}Cl_x$ are -4.2 eV, -3.95 eV and -3.3 eV according to Refs. [19, 23]. Compared with a-TiO_2, the CBM value of a-Nb_2O_5 is higher and closer to the CBM of the $Cs_3Sb_2I_{9-x}Cl_x$ absorber. The improvement of CBM position for a-Nb_2O_5 enhances the carrier extraction and transport capability at the a-Nb_2O_5/$Cs_3Sb_2I_{9-x}Cl_x$ interface, which improves the V_{oc} value of the cell [24-26].

To understand the enhanced photovoltaic performance, the typical J-V features of the $Cs_3Sb_2I_{9-x}Cl_x$ cells with a-TiO_2 and a-Nb_2O_5 were analyzed in depth. Fig. 8c displays the corresponding dark J-V curves. It is clear that the device with a-Nb_2O_5 has a much lower leak current in contrast to the device with a-TiO_2, hinting that the recombination of charge carriers is restrained significantly, which results in the improvement of V_{oc}, J_{sc} and FF in device. These results are consistent with the illuminated J-V measurement results [27].

Fig. 8d indicates the dependence of V_{oc} on different light intensities. As shown in Fig. 8d, $Cs_3Sb_2I_{9-x}Cl_x$ cell with a-Nb_2O_5 indicates a less loss of V_{oc} with the reduction of light intensity in comparison to a-TiO_2-based device. The trap-assisted recombination probability can be obtained through ideal factor (n) with the equation: V_{oc}=nkTln(I)/e+constant (k, T, and e are the Boltzmann constant, absolute temperature, and elementary charge, separately) [7, 28, 29]. Compared with the solar cell with a-TiO_2, the solar cell with a-Nb_2O_5 has a lower n value of 1.374. The reduced n value for a-Nb_2O_5-based device suggests a suppressed trap-assisted recombination, which is beneficial to enhance the V_{oc}, J_{sc} and FF of device [30, 31].

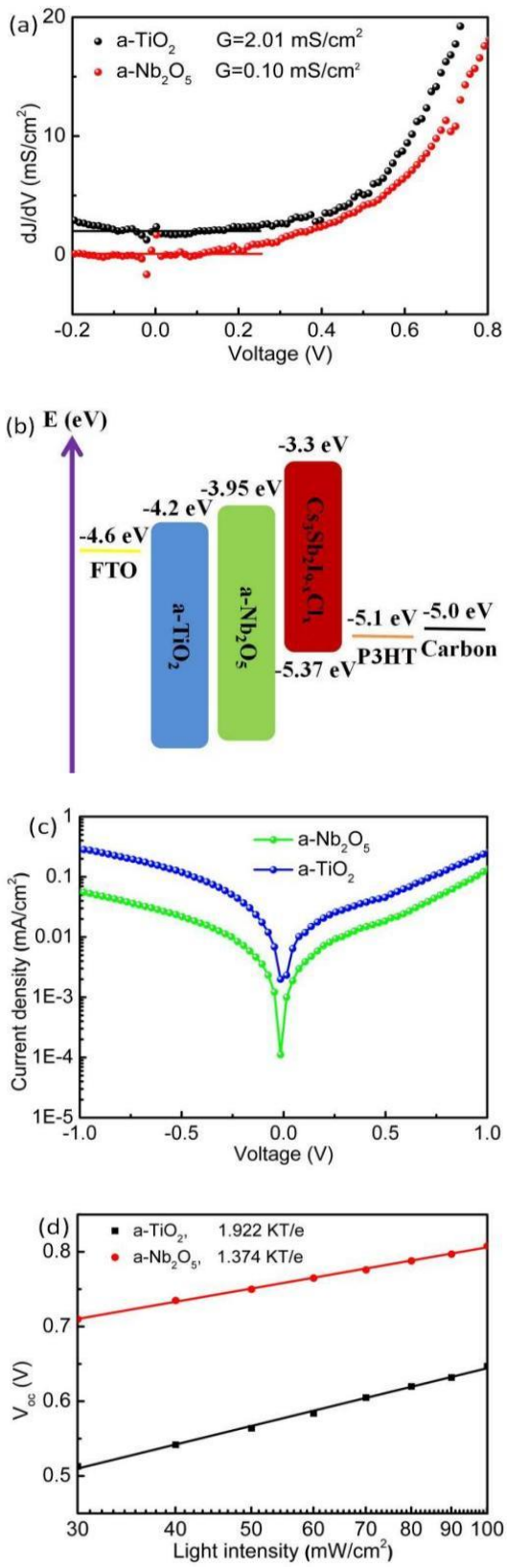

Fig. 8. (a) Plot of dJ/dV vs V. (b) The energy band diagrams of the whole device. (c) J-V curves of the cells based on a-TiO_2 and a-Nb_2O_5 under dark condition. (d) V_{oc} for the cells with various ETLs as a function of light intensity (color online)

The enhanced stability under moisture attack is equally important for the commercial applications of PSCs [32, 33]. To get more highlights into the humidity tolerance of these antimony-based solar cells, the photovoltaic performances of unencapsulated solar cells including a-TiO_2 and a-Nb_2O_5 ETLs are tested under air condition with ~40% humidity for 7 days. As seen in Fig. 9, the device comprising a-TiO_2 remain nearly 80% of initial efficiency after 7 days, displaying the good moisture tolerance. After using a-Nb_2O_5, there is obvious positive effect on the durability of corresponding cell. The all-inorganic antimony-based solar cells with a-Nb_2O_5 remain 88% of initial efficiency after 7 days, demonstrating the advantages to facilitate device properties. Our results reveal that a-Nb_2O_5 ETLs are expected to significantly improve the photovoltaic properties and environmental tolerances of all-inorganic lead-free antimony-based solar cells.

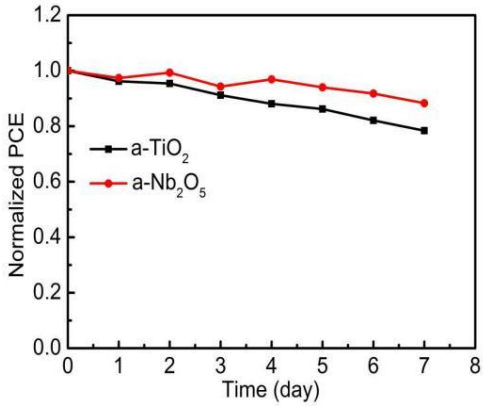

Fig. 9. Stability of two devices stored in air at room temperature (color online)

4. Conclusions

In summary, a room-temperature sputtered a-Nb_2O_5 ETL for all-inorganic lead-free $Cs_3Sb_2I_{9-x}Cl_x$ perovskite-like solar cell was proposed. It can be seen that the best-performing $Cs_3Sb_2I_{9-x}Cl_x$ cell including a-Nb_2O_5 ETL achieved a higher efficiency (1.75 %) with reduced charge recombination and leakage current, compared with a-TiO_2 based device (0.69 %). The suitable optical bandgap and high CBM are also responsible for the improved efficiency. Meanwhile, the prolonged $Cs_3Sb_2I_{9-x}Cl_x$ device stability is achieved. The results of this study highlights the importance of optimizing the ETL and interface properties, and provides a room-temperature process for the realization of efficient and stable lead-free $Cs_3Sb_2I_{9-x}Cl_x$ solar cell.

Acknowledgements

This work was supported by the Major State Basic Research Development Program of China (Grant No. 2013CB922300), the National Natural Science Foundation of China (Grant No. U1802257), Spring City Plan: the High-level Talent Promotion and Training Project of Kunming (2022SCP005) and the Young Talent Program of Changzhou Institute of Technology (Grant No. 31020222006).

References

[1] A. Hiltunen, N. Lamminen, H. Salonen, M. Liu, P. Vivo, Sustain. Energ. Fuels **6**, 217 (2022).
[2] Y. Guo, H. Lei, L. Xiong, B. Li, G. Fang, J. Mater. Chem. A **6**, 2157 (2018).
[3] P. Kumar, K. Ahmad, J. Dagar, E. Unger, S. M. Mobin, Chem. Electro. Chem. **8**, 3150 (2021).
[4] K. Ahmad, M. A. Shinde, G. Song, H. Kim, Ceram. Int. **47**, 34297 (2021).
[5] Z. Wang, D. P. McMeekin, N. Sakai, S. Reenen, K. Wojciechowski, J. B. Patel, M. B. Johnston, H. J. Snaith, Adv. Mater. **29**, 1604186 (2017).
[6] Z. Chen, M. Yang, R. Li, Z. Zang, H. Wang, Adv. Optical Mater. **10**(18), 2200802 (2022).
[7] J. Duan, Y. Zhao, X. Yang, Y. Wang, B. He, Q. Tang, Adv. Energy Materials **8**(31), 1802346 (2018).
[8] H. Yuan, Y. Zhao, J. Duan, Y. Wang, X. Yang, Q. Tang, J. Mater. Chem. A **6**, 24324 (2018).
[9] J. Ding, Y. Zhao, J. Duan, B. He, Q. Tang, Chem. Sus. Chem. **11**, 1432 (2018).
[10] Z. Liu, B. Sun, X. Liu, J. Han, H. Ye, T. Shi, Z. Tang, G. Liao, Nano-Micro Lett. **10**, 34 (2018).
[11] A. Singh, K. M. Boopathi, A. Mohapatra, Y. F. Chen, G. Li, C. W. Chu, ACS Appl. Mater. Interfaces **10**, 2566 (2018).
[12] F. Umar, J. Zhang, Z. Jin, I. Muhammad, X. Yang, H. Deng, K. Jahangeer, Q. Hu, H. Song, J. Tang, Adv. Optical Mater. **7**, 1801368 (2019).
[13] D. Shen, W. Zhang, Y. Li, A. Abate, M. Wei, ACS Appl. Nano Mater. **1**, 4101 (2018).
[14] Y. Guo, J. Zhou, F. Zhao, Y. Wu, J. Tao, S. Zuo, J. Jiang, Z. Hu, J. Chu, Nano Energy **88**, 106281 (2021).
[15] F. Zhao, Y. Guo, X. Wang, J. Tao, Z. Li, D. Zheng, J. Jiang, Z. Hu, J. Chu, Journal of Alloys and Compounds **842**, 155984 (2020).
[16] Y. Xiang, Z. Ma, J. Zhuang, H. Lu, C. Jia, J. Luo, H. Li, X. Cheng, J. Phys. Chem. C **121**, 20150 (2017).
[17] F. Zhao, Y. Guo, X. Wang, J. Zhou, J. Tao, D. Zheng, J. Jiang, Z. Hu, J. Chu, Journal of Alloys and Compounds **860**, 157900 (2021).
[18] S. Cao, H. Wang, H. Li, J. Chen, Z. Zang, Chem. Eng. J. **394**, 124903 (2020).
[19] F. Zhao, J. Zhou, J. Tao, Y. Guo, J. Jiang, J. Chu, Journal of Alloys and Compounds **897**, 162741 (2022).
[20] Y. Guo, F. Zhao, X. Wang, J. Tao, D. Zheng, J. Jiang, Z. Hu, J. Chu, Sol. Energy Mater. Sol. Cells **221**, 110918 (2021).
[21] J. Zhou, F. Zhao, J. Shen, Y. Zhou, Y. Wu, Y. Guo, J. Jiang, J. Chu, J. Mater. Chem. C **9**, 15301 (2021).
[22] X. Lu, B. Xu, X. Qin, Y. Chen, P. Yang, J. Chu, L. Sun, ACS Appl. Mater. Interfaces **12**, 58060 (2020).
[23] Y. Guo, F. Zhao, Z. Li, J. Tao, D. Zheng, J. Jiang, J. Chu, Org. Electron. **83**, 105731 (2020).
[24] Y. Xu, J. Duan, X. Yang, J. Du, Y. Wang, Y. Duan, Q. Tang, J. Mater. Chem. A **8**, 11859 (2020).
[25] H. Wang, S. Cao, B. Yang, H. Li, M. Wang, X. Hu, K. Sun, Z. Zang, Sol. RRL **4**, 1900363 (2020).
[26] X. Li, J. Yang, Q. Jiang, H. Lai, S. Li, J. Xin, W. Chu, J. Hou, ACS Nano **12**, 5605 (2018).
[27] W. Zhu, Z. Zhang, W. Chai, Q. Zhang, D. Chen, Z. Lin, J. Chang, J. Zhang, C. Zhang, Y. Hao, Chem. Sus. Chem. **12**, 2318 (2019).
[28] F. Bu, B. He, Y. Ding, X. Li, X. Sun, J. Duan, Y. Zhao, H. Chen, Q. Tang, Sol. Energy Mater. Sol. Cells **205**, 110267 (2020).
[29] D. Wang, W. Li, Z. Du, G. Li, W. Sun, J. Wu, Z. Lan, ACS Appl. Mater. Interfaces **12**, 10579 (2020).
[30] S. K. Karunakaran, G. M. Arumugam, W. Yang, S. Ge, S. N. Khan, Y. Mai, X. Lin, G. Yang, Sol. RRL **4**, 2000390 (2020).
[31] H. Yuan, Y. Zhao, J. Duan, B. He, Z. Jiao, Q. Tang, Electrochim. Acta **279**, 84 (2018).
[32] X. Liu, X. Tan, Z. Liu, H. Ye, B. Sun, T. Shi, Z. Tang, G. Liao, Nano Energy **56**, 184 (2019).
[33] Y. Liu, B. He, J. Duan, Y. Zhao, Y. Ding, M. Tang, H. Chen, Q. Tang, J. Mater. Chem. A **7**, 12635 (2019).

*Corresponding author: fzhaobs@126.com; pzhyang@hotmail.com